

Seeing Galaxies through Thick and Thin. III. Hubble Space Telescope  
Imaging of the Dust in Backlit Spiral Galaxies

William C. Keel – University of Alabama  
Raymond E. White III – University of Alabama

Deposited 09/17/2018

Citation of published version:

Keel, W., White III, R. (2001): Seeing Galaxies through Thick and Thin. III. Hubble Space Telescope Imaging of the Dust in Backlit Spiral Galaxies. *The Astronomical Journal*, 121(3). DOI: [10.1086/319386](https://doi.org/10.1086/319386)

## SEEING GALAXIES THROUGH THICK AND THIN. III. HUBBLE SPACE TELESCOPE IMAGING OF THE DUST IN BACKLIT SPIRAL GALAXIES<sup>1</sup>

WILLIAM C. KEEL<sup>2</sup> AND RAYMOND E. WHITE, III<sup>2,3</sup>

Received 2000 May 18; accepted 2000 November 20

### ABSTRACT

We present analysis of Wide Field Planetary Camera 2 imaging of two spiral galaxies partially backlit by elliptical or S0 systems in the pairs AM 1316–241 and AM 0500–620, as well as the (probably spiral) foreground system in NGC 1275. Images in *B* and *I* are used to determine the reddening curve of dust in these systems. The foreground spiral component of AM 1316–241 shows dust strongly concentrated in discrete arms, with a reddening law very close to the Milky Way mean [ $R = A_V/E(B-V) = 3.4 \pm 0.2$ ]. The dust distribution is scale-free between about 100 pc and the arm dimension, about 8 kpc. The foreground spiral in AM 0500–620 shows dust concentrated in arms and interarm spurs, with measurable interarm extinction as well. In this case, although the dust properties are less well-determined than in AM 1316–241, we find evidence for a steeper extinction law than the Milky Way mean (formally,  $R \approx 2.5 \pm 0.4$ , with substantial variation depending on data quality in each region). The shape of the reddening law suggests that at least in AM 1316–241 we have resolved most of the dust structure. In AM 0500–620 it is less clear that we have resolved most of the dust structure, since the errors are larger. In AM 0500–620, the slope of the perimeter-scale relation (associated with fractal analysis) steepens systematically when going from regions of low to high extinction. A perimeter-smoothing length test for scale-free (fractal) behavior in AM 1316–241 shows a logarithmic slope typically  $-0.4$  on 100–1000 pc scales. However, we cannot determine a unique fractal dimension from the defining area-perimeter relation, so the projected dust distribution is best defined as fractal-like. For scales above 2–4 pixels (120–250 pc), the box-counting estimate yields a fractal dimension close to 1.4, but the perimeter-area relation yields a dimension of 0.7 on large scales and inconsistent results for small scales, so that the distribution shows only some aspects of a fractal nature. In neither galaxy do we see significant regions, even on single-pixel scales in spiral arms, with  $A_B > 2.5$ . The measurements in NGC 1275 are compromised by our lack of independent knowledge of the foreground system's light distribution, but masked sampling of the absorption suggests an effective reddening curve much flatter than the Milky Way mean (but this may indicate that the foreground system has been affected by immersion in the hot intracluster gas or is inside the stellar distribution of NGC 1275). The bright blue star clusters trace the absorption in this system quite closely, indicating that these clusters belong to the foreground system and not to NGC 1275 itself.

*Key words:* dust, extinction — galaxies: ISM — galaxies: spiral

### 1. INTRODUCTION

The importance of dust extinction within galaxies is a fundamental problem for a wide range of issues. It affects the extragalactic distance scale through inclination corrections to the Tully-Fisher relation. Dust extinction affects the inferred evolution of quasars (the high-redshift cutoff, in particular) via cumulative extinction by foreground galaxies along typical lines of sight. Estimates of star formation rates and mass-to-light ratios for individual galaxies are strongly dependent on estimates of internal absorption in galaxies. Assessing the “typical” extinction within spiral galaxies has proven controversial, and various approaches give substantially different results (and the various interpretations of these results diverge even more widely). Although the presence of obscuring matter was clear from the earliest system-

atic galaxy photography (Curtis 1918), only much later was the connection between inclination and surface brightness used to estimate how much internal extinction there might be (Holmberg 1958). Holmberg's reassuring conclusion, that internal extinction is not a major factor in the global emerging light from spiral galaxies, eventually came to be challenged on two grounds. Disney, Davies, & Phillipps (1989) showed that the blue colors and inclination behavior of spiral disks could be consistent with models of high optical depth, so that what we see is dominated by a small proportion of unreddened starlight. Valentijn (1990) drew attention to this issue by analyzing the surface brightness and inclination of spirals in the ESO-LV catalog (Lauberts & Valentijn 1989) and claiming that these quantities are empirically so independent that typical spirals must be optically thick to blue light across much of their visible disks. This analysis (though not necessarily its conclusion) was challenged by Burstein, Haynes, & Faber (1991), who attributed Valentijn's main result to possible selection effects in the galaxies included in the ESO-LV sample and asserted that the problem could be solved only when truly volume-limited galaxy samples could be assembled.

Because of the assumptions required in using these model-based techniques to estimate extinctions, we have pursued a more direct approach: observing overlapping

<sup>1</sup> Based on observations with the NASA/ESA *Hubble Space Telescope* obtained at the Space Telescope Science Institute, which is operated by the Association of Universities for Research in Astronomy, Inc., under NASA contract NAS 5-26555.

<sup>2</sup> Department of Physics and Astronomy, University of Alabama, Box 870324, Tuscaloosa, AL 35487.

<sup>3</sup> NASA Goddard Space Flight Center, Laboratory for High Energy Astrophysics, Code 662, Greenbelt, MD 20771.

galaxy pairs to measure dust extinction in foreground spirals via differential surface photometry. As set out in White & Keel (1992), the ideal pair for such an analysis has a foreground spiral galaxy half projected against a similarly sized background elliptical galaxy. This geometry allows us to recover estimates of the light from each galaxy by itself, using symmetry from the nonoverlapping portions of the images and thence to reconstruct the absorption in the overlapping part of the foreground spiral galaxy, limited only by the level of asymmetry in the spiral galaxy (since elliptical and S0 systems are so precisely symmetric). An extensive ground-based program (White, Keel, & Conselice 2000, hereafter WKC; White, Keel, & Conselice 1996; Keel & White 1995) identified the best candidates for such analysis and measured disk opacities for 10 spiral galaxies. The general results were the following:

1. Spiral arms and resonance rings can have large optical depths ( $\tau_B > 2$ ) over a wide range of galactocentric distance.
2. Interarm dust has a roughly exponential distribution with radius, and causes only mild extinction in the outer disk (typically  $A_B \geq 0.5$  only within  $0.4R_{25}$ ).
3. The extinction ratios from  $B$  to  $I$  passbands are grayer than the mean Milky Way curve, which we interpreted as evidence of patchy or clumpy extinction on scales of unresolved size.

This last point made it especially desirable to measure dust properties on finer spatial scales, perhaps recovering the intrinsic reddening curve of the material and facilitating a comparison between grain populations in various spiral galaxies. This was pursued using two approaches. We describe here high spatial resolution observations achieved by *Hubble Space Telescope* (*HST*) imaging of two especially amenable galaxy pairs, AM 1316–241 and AM 0500–620 (plus archival data on the backlit high-velocity system in NGC 1275). A complementary analysis, comparing far-IR and submillimeter emission with optical absorption measures for three overlapping galaxy pairs (including AM 1316–241) was presented by Domingue et al. (1999).

These galaxy pairs were selected as the most promising cases for symmetry and angular size from the initial survey reported by WKC. The two newly observed pairs were both initially cataloged by Arp & Madore (1987). AM 1316–241 (ESO 508-IG45) consists of a highly inclined spiral galaxy in front of an elliptical galaxy with very nearly circular isophotes, as measured from the nonoverlapping regions. The spiral has measured redshift  $cz = 10,365 \text{ km s}^{-1}$ , notably larger than that of the elliptical ( $9700 \text{ km s}^{-1}$ ; White & Keel 1992; Donzelli & Pastoriza 2000). AM 0500–620 (ESO 119-IG27) consists of a nearly face-on spiral galaxy of type Sb partially projected in front of a smooth system with a light profile suggesting an S0 classification. Donzelli & Pastoriza list heliocentric velocities of  $9005$  and  $8811 \text{ km s}^{-1}$  for the spiral and elliptical components, respectively. For linear scales, we adopt a Hubble constant of  $75 \text{ km s}^{-1} \text{ Mpc}^{-1}$ , for which a single Wide Field Planetary Camera 2 (WFPC2)  $0''.1$  pixel subtends  $65$  and  $57 \text{ pc}$ , respectively, in AM 1316–241 and AM 0500–620. We also consider archival WFPC2 data on the object in the foreground of NGC 1275; in this case the foreground system has redshift  $cz = 8200 \text{ km s}^{-1}$ , while NGC 1275 itself has  $cz = 5264 \text{ km s}^{-1}$ . Given their context in the Perseus-A426 cluster, the line-of-sight separation of

these two galaxies is almost indeterminate. Some suggest that the two galaxies are strongly interacting, perhaps enhancing the luminosity of the emission-line filaments around NGC 1275 proper (Hu et al. 1983), and absorption geometry indicates that the foreground system must lie at least outside these filaments (Keel 1983). For the PC CCD, which encompasses most of the foreground absorption, the image scale in this case is  $15 \text{ pc pixel}^{-1}$ , although we worked with mosaicked data at  $30 \text{ pc pixel}^{-1}$ .

## 2. DATA AND IMAGE ANALYSIS

The two overlapping elliptical galaxy–spiral galaxy pairs AM 0500–620 and AM 1316–241 were observed with WFPC2 in the  $B$  (F450W) and  $I$  (F814W) passbands, with the root names u3lw04 and u3lw03, respectively, for the image sequences. In each case, the total exposures were  $2000 \text{ s}$  ( $I$ ) and  $2600 \text{ s}$  ( $B$ ), split into halves for cosmic-ray recognition and rejection. The individual exposures in each filter were combined using the CRREJ task in STSDAS for cosmic-ray removal, plus cleaning “by hand” for a few particle events missed by the automated procedure. Additional  $120 \text{ s}$   $B$  and  $60 \text{ s}$   $I$  exposures were taken in case the galaxy nuclei saturated on the longer exposures, as indeed happened in  $I$  for a  $1.0'' \times 0.5''$  region at the center of the elliptical galaxy in AM 1316–241. Both members of AM 0500–620 fitted comfortably in the WF3 CCD field, while AM 1316–241 stretched across both WF2 and WF3, with WF2 containing the outer end of the foreground disk. Images in both filters were registered to within  $0.2$  pixels, so we compare the two passbands without any pixel interpolation.

As often happens, the WFPC2 images reveal significant structures in the background galaxies that were not at all apparent from our ground-based imagery. Fortunately, these have at most a slight impact on our ability to do the image modeling required for an opacity measurement. The background galaxy in AM 0500–620 (Fig. 1) now shows a central spiral pattern spanning the innermost  $2''.6 = 1.4 \text{ kpc}$ , including dust lanes and bright knots (of the appropriate luminosity to be star clusters, at  $B = 20.3$  or  $M_B = -15$  and fainter). We therefore cannot measure foreground absorption this close to the nucleus, since it is unclear which galaxy is associated with a particular small dust feature. The elliptical galaxy in AM 1316–241 (Fig. 2) has a small linear bright feature, perhaps an edge-on stellar disk, spanning a diameter of  $1''.3 = 0.8 \text{ kpc}$  and aligned in roughly the same direction as the foreground spiral disk. This structure has no effect on our measurements of dust in the foreground galaxy.

As described by WKC, our opacity measurements require modeling of the intrinsic light distributions of both foreground and background galaxies in a region where they overlap. In such a region of overlap, if the background galaxy has an unabsorbed intensity  $I_B$ , the foreground galaxy contributes an intensity  $I_F$ , and the total observed intensity is  $I$ , then the effective optical depth  $\tau$  through the foreground galaxy is

$$e^{-\tau} = \frac{I - I_F}{I_B}. \quad (1)$$

In general, we of course cannot directly separate foreground from background emission in regions where the two galaxies are superposed. We instead estimate  $I_F$  and  $I_B$  from

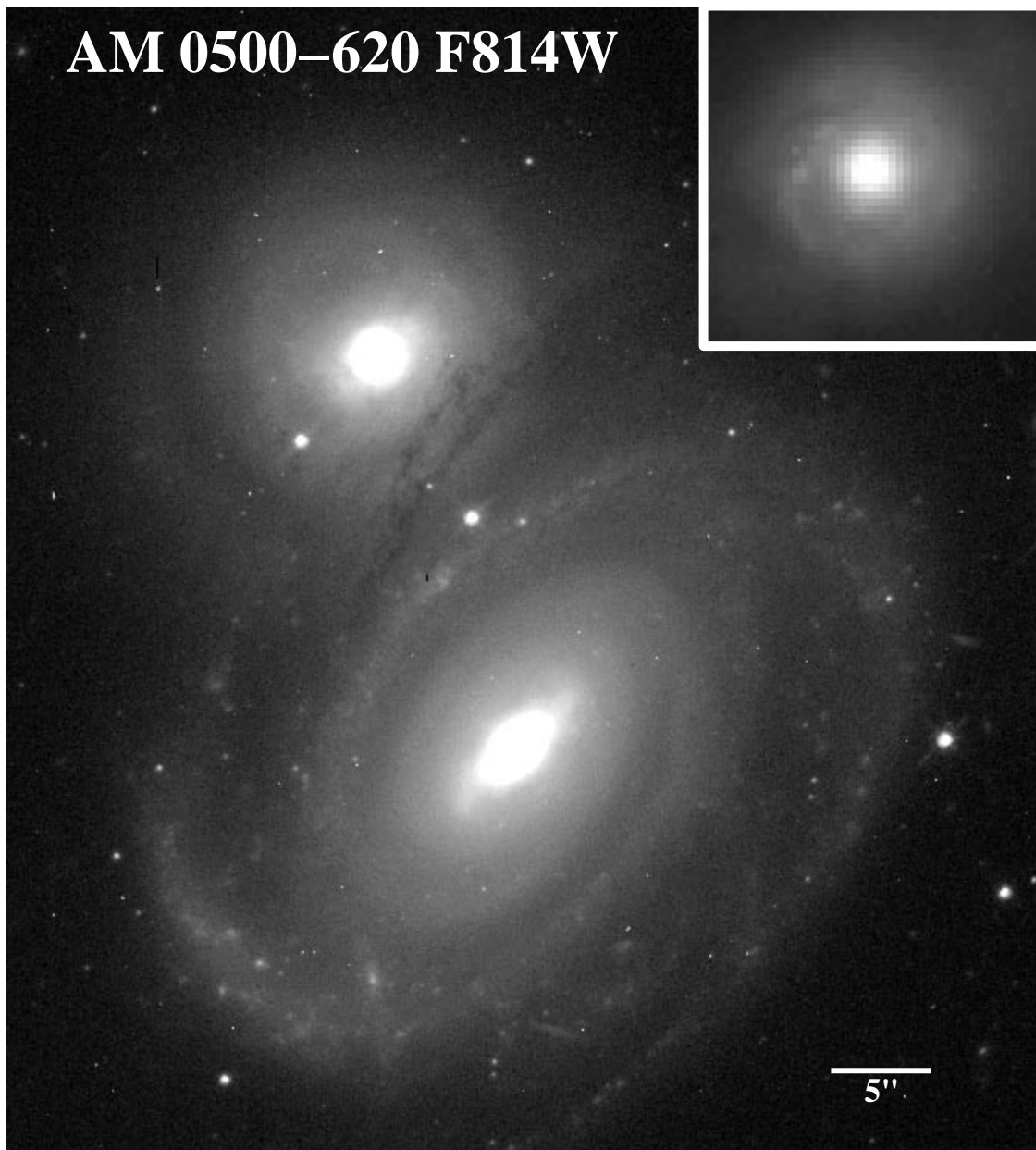


FIG. 1.—F814W image of AM 0500–620, displayed with a logarithmic transfer function to enhance visibility of the dust lanes silhouetted in front of the northern galaxy, showing the center of the background system expanded by a factor of 4 and illustrating its spiral dust lanes and star clusters (*inset*). The area shown subtends  $56'' \times 62''$ , and celestial north is  $22^\circ$  clockwise from the top. All images are shown in positive contrast to avoid confusion in interpreting absorption features.

symmetric, nonoverlapping regions of the galaxies. The two pairs we consider here were selected to be the best pairs known for such an analysis, based on angular size and symmetry of both pair members and the improved modeling that is possible if each galaxy is about half-overlapping, leaving the other half as a symmetric template. For background elliptical or S0 galaxies, estimates of  $I_B$  are especially accurate (to better than 1%) since we can make a two-dimensional symmetric model based on all parts of the galaxy that are unlikely to be overlapped by any material associated with the foreground galaxies. In practice, stars, background galaxies, and any other fine structures are masked during model fitting. Residuals from the fit can be evaluated in the nonoverlapping areas, giving us a point-by-point assessment of how accurate the modeling has been.

We perform these operations in the observed pixel frame without any rebinning, which would degrade resolution in some parts of the field of view.

In the case of NGC 1275, the foreground system and intrinsic structures cover enough area that several rounds of masking were needed to get a smooth symmetric background model. We used symmetry to provide an initial guess at intensities in the area not imaged around the PC chip, as needed by the STSDAS ELLIPSE routine to provide a large enough fraction of the elliptical isophotes in some ranges of the semimajor axis.

Larger errors will be introduced through uncertainties in the foreground galaxy intensity  $I_F$ , since spirals are rich in structure. AM 0500–620 is attractive for this analysis since its “grand design pattern” is highly symmetric; the ridge-

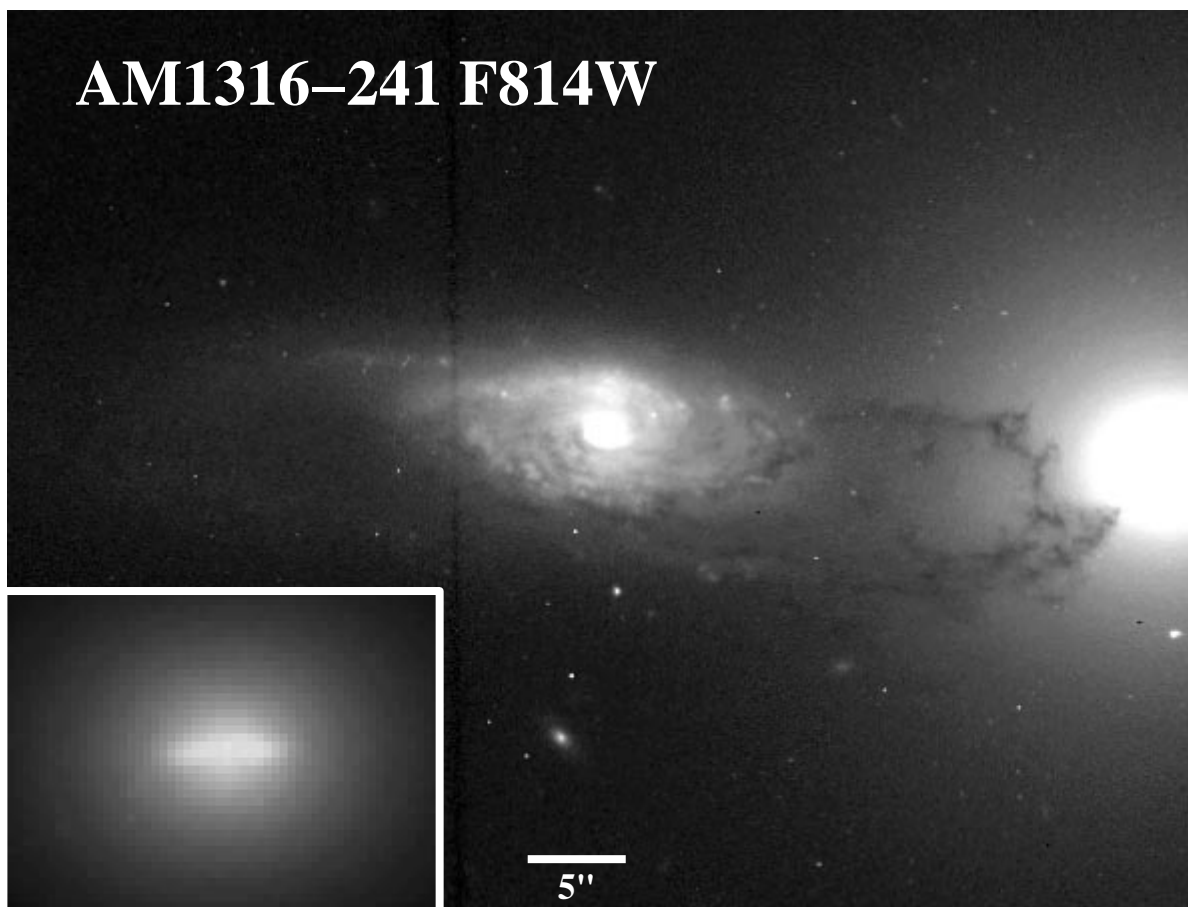


FIG. 2.—F814 image of AM 1316–241, displayed with a logarithmic intensity scale, showing the nuclear disk structure in the background elliptical galaxy at a scale 4 times larger (*inset*). The field shown here is  $45'' \times 70''$  from WFPC2 chips 2 and 3, where north is  $58^\circ$  clockwise from the top. For display purposes, data from the two CCDs have been resampled to a common astrometric grid by using the WMOSAIC task in STSDAS, but no such resampling was done for the numerical analysis.

lines of its spiral pattern lie within  $1''$  of their mirror reflections. Our point of departure for modeling it was rotation through  $180^\circ$  with median filtering with an 11 pixel ( $1''.1$ ) square window to remove bright clusters and associations, so we need to deal only with positive structural residuals and subtraction. In AM 1316–241, the opposing outer arm at the relevant radius is both smooth and of rather low surface brightness, so that it does not offer a large uncertainty in accounting for foreground light if the spiral is even roughly symmetric at these radii. It proved useful to model the galaxies in each pair iteratively, using a first-guess model of the background galaxy to isolate emission from the foreground galaxy, subtract this from the data, derive an improved background model, and so on. Scatter in the residuals indicates that the errors in  $e^{-\tau}$  are 0.11–0.15 per pixel in  $I$  for AM 0500–620 and somewhat better, 0.06–0.10, for AM 1316–241; photon statistics and systematic errors from structure in the foreground galaxies contribute about equally to the error budget. The foreground corrections range from 5% to 30% in AM 1316–241 and from 2% to 15% in AM 0500–620, so that departures from symmetry in the foreground light distribution will be multiplied by these factors in their impact on derived opacity values.

Scattering of background galaxy light by dust in the foreground galaxy could reduce the effective optical depth we measure. Numerical integrations to estimate this effect,

starting from plausible line-of-sight separations between the galaxies, were described by WKC, and these remain valid for the new data. The relevant quantity is not the fractional amount of scattered light itself but the differential scattering between the point under consideration for opacity measurement and its symmetric counterpart in the foreground disk that was used to estimate  $I_F$ . For these pairs, this effect is small: less than 3% for AM 0500–620 and less than 1% for AM 1316–241.

Realization of equation (1) for these images yields maps of residual intensity,  $e^{-\tau}$ , as shown in Figures 3–5. We work primarily with residual intensity (transmission), denoted  $T_B$  and  $T_I$ , rather than optical depth  $\tau$  or magnitudes of extinction  $A_B$  and  $A_I$  for statistical measurements because the errors in this linear quantity are much better behaved (being symmetrically distributed) than in the logarithmic measures. In both systems, the  $I$  data are of higher quality than the  $B$  despite the smaller extinction at  $I$ , resulting from the better  $S/N$  ratio of the initial data, the better symmetry, and reduced influences of young clusters and associations in the redder passband.

### 3. DISTRIBUTION OF DUST ABSORPTION

The spiral components of these pairs offer interesting distinctions, suggesting some of the variety that must be present among spiral galaxies. The dust in AM 1316–241 is very strongly concentrated in the prominent arm, now seen

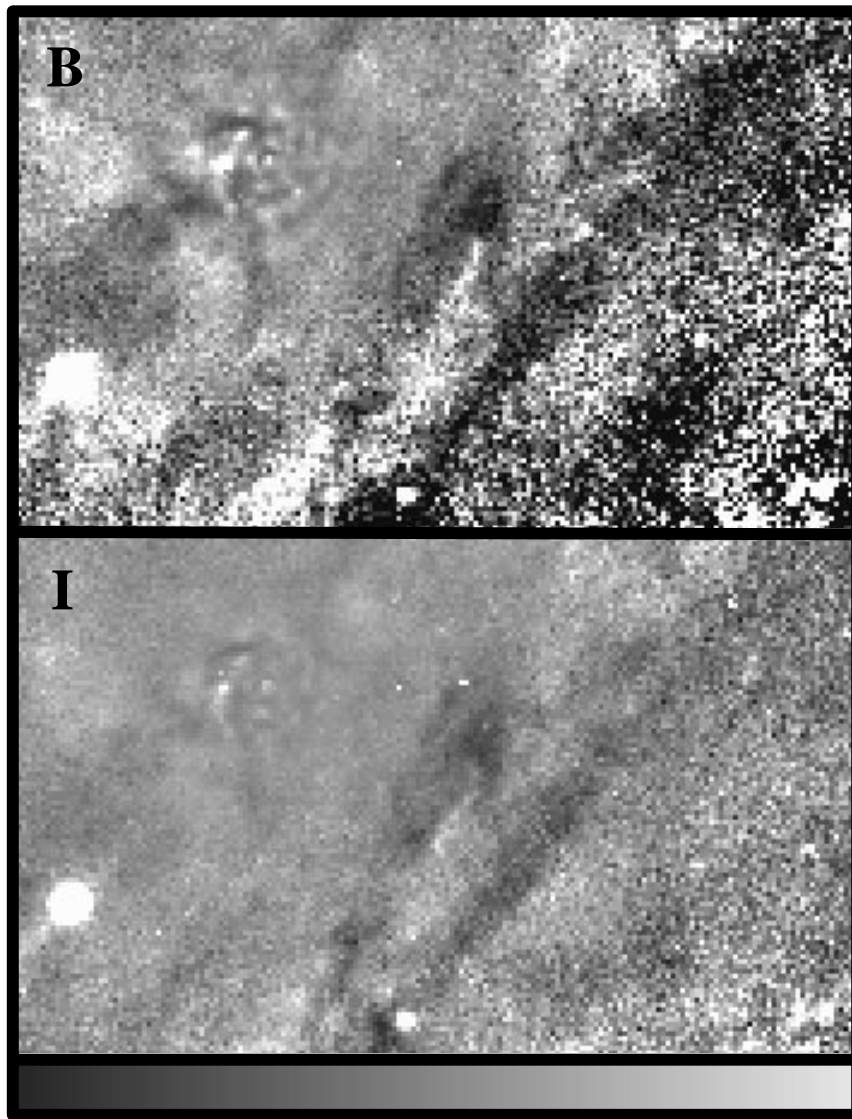


FIG. 3.—Transmission maps of the overlap region of AM 0500–620 in *B* and *I* bands, displayed at the same intensity scale. The region depicted subtends  $10''.7 \times 17''.5$ , showing structure near the nucleus of the background galaxy (*upper left*). The intensity scale bar is linear from 0 to 1.5. Two spiral arms and an interarm dust spur are prominent in absorption. The cloud examined for reddening behavior in Fig. 12 is just above the center of each panel.

as a rich filamentary pattern, with none seen outside this arm (to quite low limits) and only a small amount inside the arm (until the background intensity has dropped too low to allow measurement of dust in the next spiral feature inward). In AM 0500–620, there are several very narrow spiral features outlined by dust, including a spur between two of the prominent arms, plus a significant component of interarm obscuration. The arm-interarm distinction that proved useful in ground-based work remains valid at this increased resolution and is in fact even clearer. At all projected radii that we can sample, we see a strong distinction between dust in spiral arms and spurs on the one hand and more smoothly distributed interarm dust on the other. The regions we can usefully analyze span the range  $(0.53\text{--}0.72)R_{25}$  in AM 0500–620 and  $(0.44\text{--}0.80)R_{25}$  in AM 1316–241.

One global description of absorption effects is the fraction of area covered at various extinction values. Figure 6 shows both differential and cumulative distributions of

area as functions of transmission  $T_B$  for the regions in AM 1316–241 and AM 0500–620 that are well measured. The two are different in detail. In particular, AM 0500–620 has a larger fraction of area with low opacity than AM 1316–241; furthermore, AM 1316–241 has an obviously bimodal distribution of opacity, while AM 0500–620 does not. Half the area in AM 1316–241 is covered by dust with a *B* transmission of  $T_B = 0.63$  or greater, while the corresponding halfway point in AM 0500–620 is  $T_B \geq 0.82$ . Typical pixel-by-pixel errors are 0.1 in transmission, as shown by the width of the spike near zero extinction ( $T_B = 1$ ) in AM 1316–241, so that the number of points with  $T_B < 0.1$  is consistent with scatter from points higher in the distribution, so that we see no evidence for pixel-scale areas passing less than 10% of the light ( $A_B > 2.5$ ). These distributions are clearly area weighted rather than intensity weighted, so these kinds of measures are useful in coverage problems such as evaluating the effect of galaxy disks in absorbing quasar light.

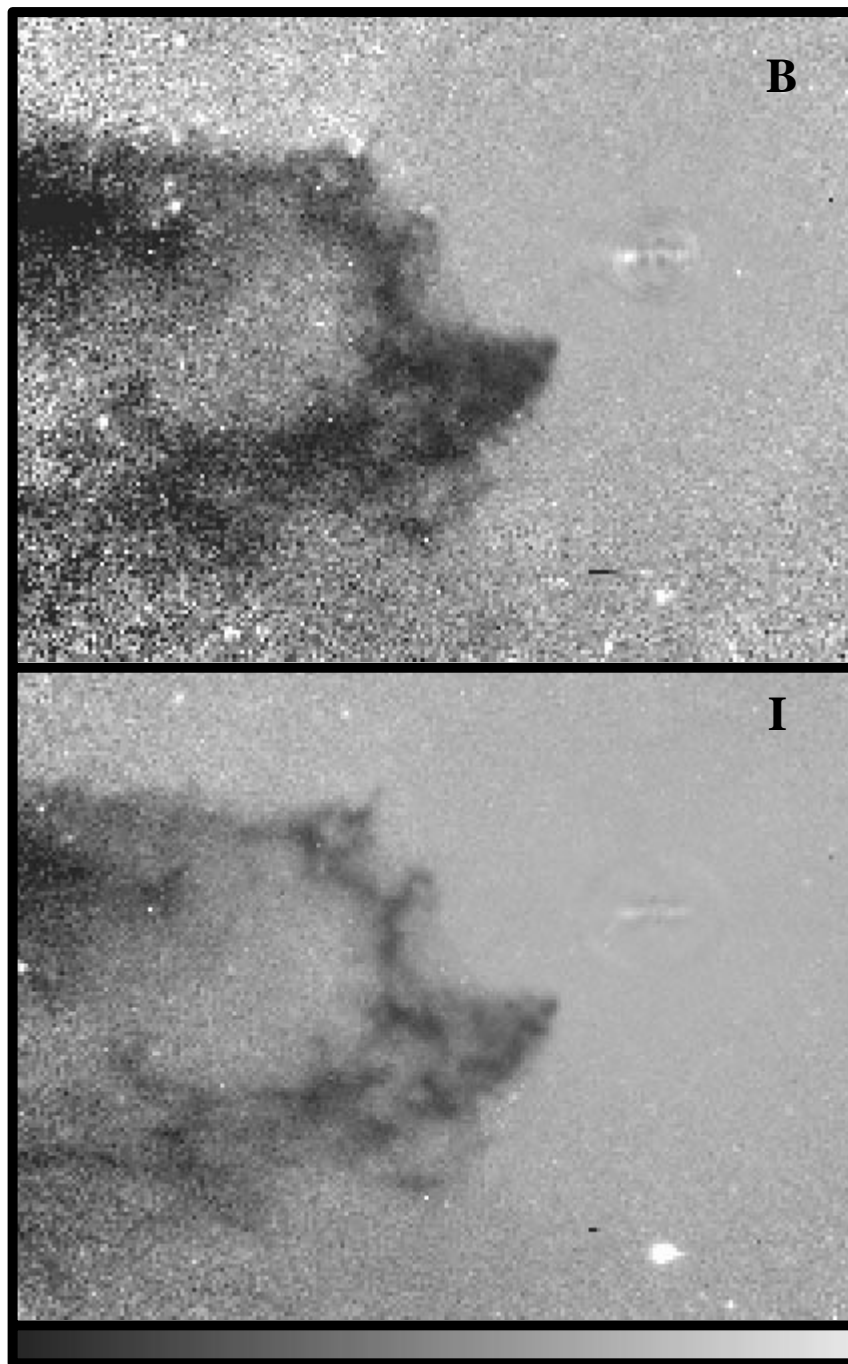


FIG. 4.—Same as Fig. 3, but for AM 1316–241. Each panel shows a region  $21''.0 \times 16''.1$ . The intensity scale bar is linear from 0 to 1.5. The apparent edge-on nuclear disk in the background elliptical galaxy appears at right. There is very little absorption signature within the prominent and filamentary spiral feature.

We use the compromise dust mixture from Domingue et al. (1999) to estimate the dust mass seen in these regions and compare arm and interarm contributions. This mixture (about midway between pure graphite and pure silicate grains in their optical properties and density) has mass column density  $\rho = (2.41 \times 10^{-5})\tau_B \text{ g cm}^{-2}$ , or  $0.12\tau_B M_\odot \text{ pc}^{-2}$ . The transmission maps can thus be turned into column density maps for each overlapped area. As a guide in interpreting the figures,  $\tau = 1$  in the *I* images corresponds to a dust mass per pixel of  $900 M_\odot$  in AM 0500–620 and  $1166 M_\odot$  in AM 1316–241.

In AM 0500–620, the arm-interarm contrast is much higher than we saw from the ground in WKC, because much of what appeared to be diffuse interarm extinction is now resolved into the prominent spur cutting across the main spiral pattern. By defining arm features at  $\tau_B \geq 0.15$ , the boundary of contiguous arm extinction, or at  $57 M_\odot$  per pixel, we find that 97% of the dust mass is in arm regions comprising 54% of the projected area. Higher column density cuts yield further relations: 55% (36%) of the dust mass is contained within 20% (10%) of the projected area. The most prominent cloud complex, above center in the

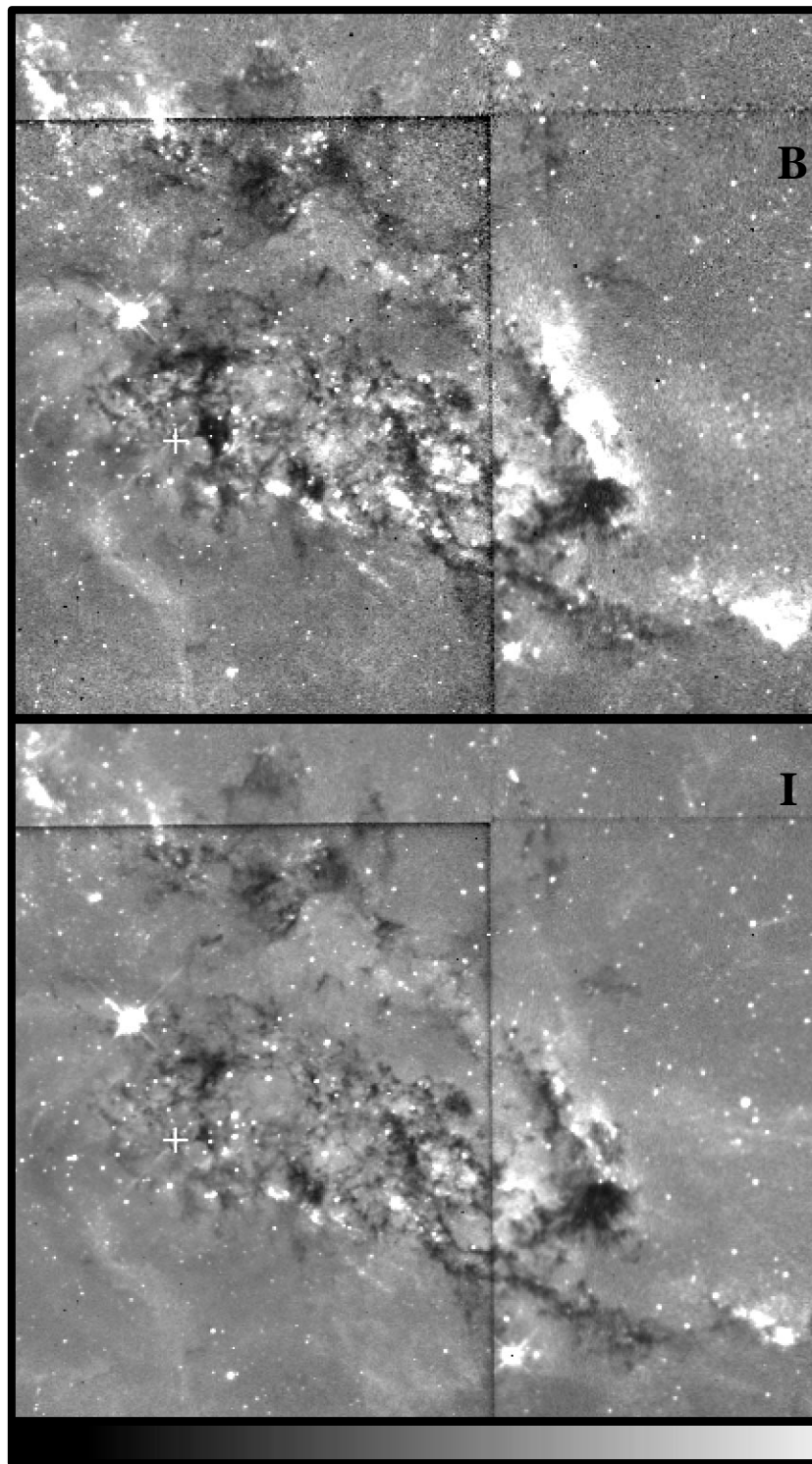


FIG. 5.—Transmission maps of the backlit foreground system in NGC 1275, now including mosaicked parts of all four WFPC2 CCDs. The bright star clusters can be seen closely associated with absorption regions, though the division by the background model needed to derive transmission values exaggerates their brightness with increasing distance from the Seyfert nucleus (*crosses*). The intensity scale (*bottom*) is linear from 0 to 1.5 in transmitted intensity. This field is  $42''.7$  across, and north is  $48^\circ$  clockwise from the top. The F450W and F702W filters transmit enough light from strong emission lines to show some of the low-ionization filaments in NGC 1275, as seen particularly at lower left in each image.

spur, has a total dust mass of about  $1.4 \times 10^5 M_\odot$ . For a typical Galactic gas-to-dust ratio of 300 by mass, this implies a total mass in the cloud of order  $4 \times 10^7 M_\odot$ , typical for a large molecular cloud complex extending almost 2 kpc in an arm.

Individual clouds are less distinct in AM 1316–241. Several individual clumps on  $0''.4$ – $0''.8$  (250–600 pc) scales have dust masses in the range  $(3\text{--}7) \times 10^4 M_\odot$ . The concentration toward the arm pattern is pronounced here as well, with 89% of the mass in the overlap region contained in

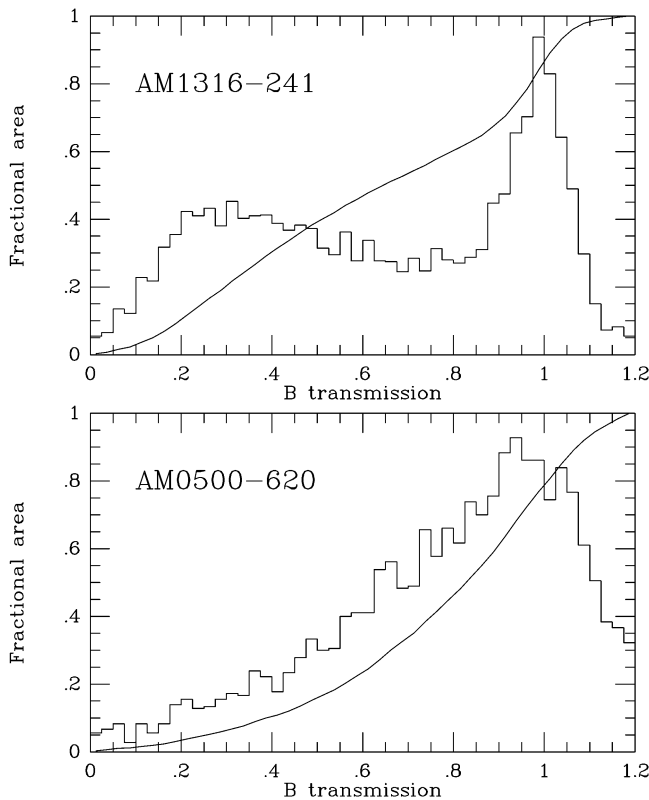


FIG. 6.—Distribution of  $B$ -band extinction by area for regions in AM 1316–241 and AM 0500–620. The regions examined are the same ones used for the fractal analysis, comprising 6617 pixels for AM 1316–241 and 3540 pixels for AM 0500–620. The smooth curves represent cumulative distributions, the fraction of the area with less than the indicated level of transmission. The heavy spiral arm and almost transparent interarm region make the differential distribution distinctly bimodal in AM 1316–241, while that in AM 0500–620 shows a monotonic (and almost uniform) decline in affected area with extinction. In each case the pixel-by-pixel area is typically 0.1, so the number of pixels below 0.1 (about 0.05) is consistent with measurement error alone; that is, these data suggest that essentially none of the regions studied have  $A_B > 2.5$  mag. For each panel, the vertical scale (*bottom*) refers to the cumulative distribution and is relative for the differential histogram.

contiguous structures occupying half the area. The 10% of the area with the highest column densities contains 31% of the dust.

Our analysis for NGC 1275 is necessarily less nearly complete than for the two AM pairs, since photometry alone cannot be used to assess independently the amount of foreground light coming from a completely backlit galaxy. We have tried to limit the impact of this uncertainty by masking all pixels bluer than a limiting value in the  $B/I$  flux ratio, which includes many pixels with obvious absorption. This leaves us unable to derive reliable covering fractions, since the blue clusters are distributed in almost the same way as the dust (frequently with a systematic offset such as those often seen between dust and stars in typical spiral arms). In fact, the distributions of blue clusters and absorption (Fig. 5) suggest that most of the bright blue clusters studied by Carlson et al. (1998) are in fact part of the foreground galaxy and not NGC 1275 itself.

Of the regions we can measure in NGC 1275,  $T_I = 0.45$  is the lowest  $I$ -band (F702W for this object) transmission found in areas large enough to be real detections; the areal distribution of  $T_I$  is nearly flat from  $T_I = 0.60$  to 0.90. The

dust lanes are about as optically thick as the spiral arms in the other two systems. However, as noted below, the extinction curve in this system is drastically different from what we find for the other two spirals. This may signify a real difference in the grain population or it may be due to the foreground galaxy’s being embedded in the “background” galaxy so that some of the near-side light from the “background” galaxy may not be absorbed by the foreground galaxy. The structures of both absorption and excess emission from blue clusters and associations strongly resemble a late-type spiral in at least the northwest half of the foreground system, as seen in Figure 5. This is in accord with several previous studies identifying this object as a late-type spiral, seen almost edge-on and perhaps being disrupted by a very rapid tidal encounter with the background galaxy (Keel 1983; Hu et al. 1983).

### 3.1. Fractal Structure in Dust Distributions?

Indications that the H I in several nearby galaxies can be modeled as scale-free fractal distributions (Westpfahl et al. 1999) motivate a similar analysis of the dust maps described above. One prominent symptom of fractal behavior is a scale-free relation between the perimeter of a contour and the scale length over which it is integrated or smoothed for the measurement. We employ a perimeter-scale test, implementing the box-counting procedure of Westpfahl et al. Specifically the length of various contours was evaluated in transmission maps for various values of  $T_I$  and for smoothing lengths of 1, 2, 4, 8, and 16 pixels, so that no resampling of pixel values affects the results. This evaluation was done by creating masked images cut above and below desired thresholds, then counting the number of pixels making the transition. We plot this relation using perimeters scaled to the original pixel size (rather than block-averaged effective pixels at each scale), so the box-counting dimensions will equal the slope of the relation plus 1.

In AM 1316–241, the perimeter-scale relation is nearly linear (in the logarithm of each quantity) over scales from 2 to 16 pixels (130 to 1000 pc) when contours are used for transmission values  $T_I = 0.5$ –0.9 on the higher quality  $I$  map (Fig. 7). The measured perimeter for 1 pixel smoothing scales (i.e., the original data) is larger than the extrapolated value from larger smoothing lengths for all transmission levels. Numerical experiments using block-averaged and point-spread function–convolved versions of the original image confirm that this discrepancy cannot be due to the numerical properties of the algorithm (which operates stepwise in exactly the same way as when going from 1 to 2 pixels, for example, from 2 to 4); this result is in the opposite sense of that of any smoothing effects due to the finite point-spread function (PSF) of WFPC2 images (which would contribute about a 20% perimeter reduction due to smoothing). However, the effects of finite signal-to-noise ratio in the data can contribute significantly to apparent structure at small opacities on scales of 1–2 pixels. The effect is most apparent for small opacity because the local slope in residual intensity is smaller, so a given amount of noise will move the contour at a particular level by a large amount. We estimate the magnitude of the effect by recomputing the area-perimeter relation for smoothing lengths of 1, 2, and 4 pixels for subsections of the AM 1316–241 dust lane selected to have different typical signal-to-noise levels. Indeed, this shows that the perimeters derived for the original data at transmission 0.9 are overestimated for a smaller signal-

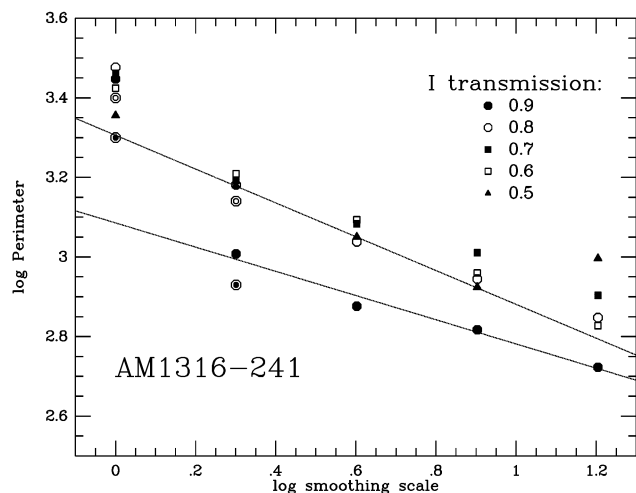


FIG. 7.—Box-counting analysis of the relation between contour length (region perimeter) and smoothing length for a 128 pixel square region in AM 1316–241. Contours were evaluated for values of  $I$  transmission from 0.5 to 0.9. Scale-free (fractal) behavior is manifested as straight lines in this log-log plot and is a good description of what is seen for smoothing scales greater than 1 pixel. The lines shown are best fits to the middle three points in the contours at levels 0.5 and 0.9 and show the apparent excess of structure for no smoothing (single-pixel scales); some of the values at large smoothing values are likely to be unreliable when small total areas are involved. This excess amounts to a factor of 2 in perimeter length above the extrapolation of the relation for the 0.9 level contour. The circled points indicate an approximate correction for a finite signal-to-noise ratio in the images, which is important only for the smallest smoothing scales and largest transmissions. Much (but not all) of the apparent discrepancy between unsmoothed and smoothed data is removed by this correction.

to-noise ratio and that the effect can approach 50% for the lowest-quality data involved. It is much smaller, never greater than 20% for smoothing scales of 2 pixels, and is negligible for 4–8 pixel smoothing. Figure 7 includes circled points incorporating these corrections, which fall closer to the linear extrapolations from larger smoothing scales. There is still some excess at single-pixel sampling, although the effects of noise are difficult to model precisely enough to tell whether this is a genuinely physical effect.

There is marginal evidence that the slope of the logarithmic perimeter-scale relation (i.e., the negative of the box-counting dimension) varies systematically with transmission, from  $-0.35$  for  $T_I = 0.8$ – $0.9$  to  $-0.42$  for  $T_I = 0.5$  (though the scatter between transmission values is substantial). This may be due to the overlap of individual structures or may reflect intrinsic properties of the distribution. Thus, while the contours at constant transmission are individually scale-free for sampling lengths  $\geq 2$  pixels, the scaling seen for different transmission values is not consistent. A slope of  $-0.4$  is representative of the whole data set for this object, leading to a box-counting dimension  $D_b = 1.4$ . As noted by Westpfahl et al. (1999), while the various ways of measuring dimension for arbitrary contours need not coincide, they are often very close for astronomical applications. A dimension  $\sim 1.4$  lies within the range 1.2–1.5 found for projected H I distributions in nearby galaxies by Westpfahl et al., so this may be a typical range for cold interstellar medium (ISM) constituents.

The traditional definition of the fractal dimension comes from Mandelbrot's equation for a group of contours at different levels but the same smoothing scale, with perimeter  $P$

and area  $A$ :

$$P^{1/D} = (\text{const})A^{1/2},$$

where the constant may take on different values for various smoothing scales. For these data, we find that the area enclosed by a contour at a given level is closely constant for various smoothing values, in fact as constant as numerical scatter will preserve (to within 10% over a factor of 8 in smoothing scale for well-sampled contours). The near-constancy of the area implies that the mass estimates derived above from absorption at the observed resolution are not significantly affected by subpixel structure. We are unable to fit a unique fractal dimension  $D$  from this relation (Fig. 8), because the observed  $\log P$ – $\log A$  relation is very nonlinear (being close to parabolic with a clear maximum). The most we can then say about the projected dust distribution in this context is that it has fractal aspects as seen in the scaling behavior of individual contours but not as seen in the whole family of contours at different levels for a given smoothing length. For large smoothing scales (4 pixels or more), the scaling behavior exhibits a slope near 0.35 in the  $(\log P, \log A)$  plane, implying a dimension 0.7 (twice the slope). This differs strongly from the box-counting dimension of 1.4, as well as being very dependent on smoothing length. The dust distribution we observe thus shows some aspects of fractal behavior but does not satisfy the Mandelbot definition for these reasons.

In AM 0500–620 the region of overlap is about 2 times smaller than that in AM 1316–241, so analysis of its geometry is necessarily sketchier. Applying the box-counting procedure to a  $64 \times 64$  pixel region shows approximate scaling behavior all the way down to single-pixel scales (Fig. 9), in contrast to what we see in AM 1316–241. These data are consistent, therefore, with a fractal or scale-free dust distribution on scales from 50 to 400 pc, while the size of the backlit region does not allow us to measure scales larger than this. However, we note that

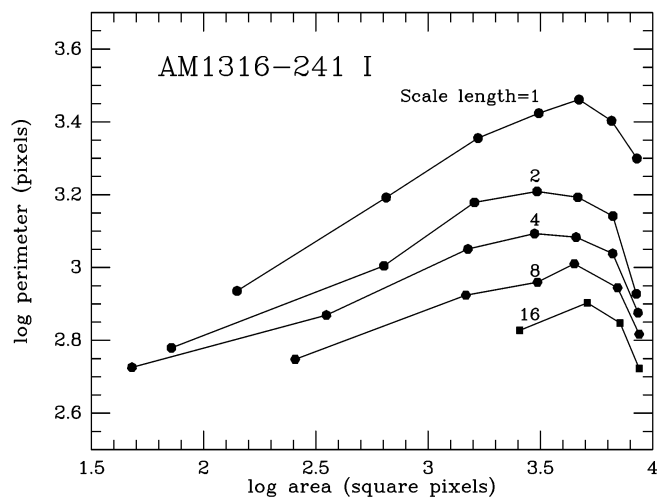


FIG. 8.—The defining area-perimeter test for fractal behavior, applied to the  $I$ -band extinction in AM 1316–241 as sliced at transmission levels from 0.5 to 0.9. A pure fractal distribution would appear as a straight line (log-log relation) in this plot, which shows the relation for each value of smoothing (1–16 pixels) with points indicating values measured at intervals of 0.1 in transmission (0.9 is at right). The same S/N corrections have been made as shown in Fig. 7; the peak and downturn at small smoothing scales persist even with no such correction.

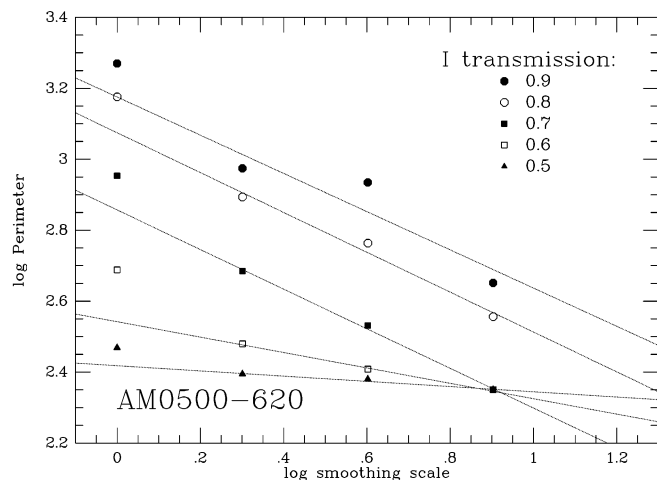


FIG. 9.—Box-counting analysis of the relation between contour length (region perimeter) and smoothing length, for a 64 pixel square region in AM 0500–620. Contours were evaluated for values of  $I$  transmission from 0.5 to 0.9 as indicated. Scale-free (fractal) behavior is manifested as straight lines in this log-log plot and is a good description of what is seen for smoothing scales greater than 1 pixel. The lines shown are best fits to each contour level, lying at the left edge in monotonically increasing order from 0.5 to 0.9. Any excess above this for single-pixel scales is marginal, distinguishing this situation from AM 1316–241. The apparent flattening of slopes and crowding of the relation for deeper contours toward the bottom are artifacts of the small number of available pixels when large smoothing scales are applied.

higher noise per pixel in this case might to some extent mimic pixel-scale structure in the contours. In contrast to AM 1316–241, the fitted slope of the logarithmic perimeter-scale relation flattens when going to larger extinction, this time from  $-0.55$  at  $T_I = 0.8$ – $0.9$  to  $-0.2$  at  $0.6$ . This is the level at which the size of the analyzed region introduces an artificial limit to the perimeter measures.

### 3.2. Fine Structure and the Reddening Law

A major goal of these observations is to quantify the effects of dust on scales finer than the kiloparsec resolutions afforded by ground-based images. In particular, we ask whether there are preferred scales for absorbing complexes or whether the spectrum of structure continues down to the WFPC2 resolution limit. Our analysis of the structure in opacity maps, described above, is one way to address these questions. In another approach, we consider how the residual (transmitted) intensities  $T_B$  and  $T_I$  are correlated pixel by pixel. Smoothly distributed dust and dust clumped in high-opacity “bricks” are two extremes for the dust distribution that lead to different predictions for the wavelength dependence of the extinction. The extinction of smoothly distributed dust should follow the grains’ intrinsic reddening law (for example, the Galactic extinction curve); alternatively, if the dust is clumped into opaque clouds the extinction curve would be “grayer” because of saturation at shorter wavelengths. Figure 10 shows the two-color extinction behavior of the dust in AM 1316–241, for the region with the highest background intensity (the same area used for the fractal analysis) and therefore the signal-to-noise ratio (S/N). The error distribution for individual points will be approximately given by the elliptical scatter for points near (1,1) in these plots, and this error is not directly dependent on the local opacity since background intensity rather than amount of absorption usually controls

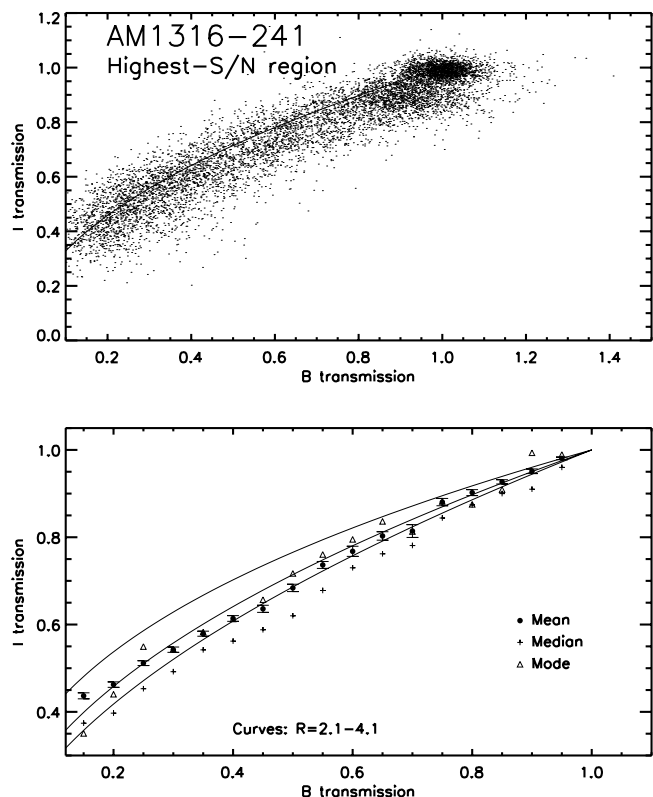


FIG. 10.—Two-band extinction relation for pixels in the part of the dust lane in AM 1316–241 with the highest S/N ratio. The upper panel shows the relation between transmission values at  $B$  and  $I$  for individual pixels, with the predicted curve for a Galactic reddening law and  $R = 3.1$  shown for reference. The lower panel shows mean, median, and mode for bins of 0.05 in  $B$  transmission, along with a family of curves generated for values of  $R = 4.1$  (lowest) to  $R = 2.1$  (highest) in steps of 0.2. Various ranges of transmission all give best-fitting values in the range  $R = 3.2$ – $3.6$ . In this and similar figures, the bottom panel is on an expanded scale to emphasize the differences expected for various values of  $R$  and the details of the data distributions.

the error. This scatter is slightly correlated between the two passbands since fine structure in the foreground galaxy will consist largely of brighter and bluer stellar associations. The lower panel shows curves predicted for  $R = A_V/E(B-V) = 2.1$ – $4.1$ . Because of the finite passbands and large extinction range involved, these curves were calculated rigorously, starting with the photon-number spectrum of a model old stellar population (using the models described by Charlot & Bruzual 1991), applying reddening using the Cardelli, Clayton, & Mathis (1989) parameterization, varying the value of  $R$ , and then folding the result through the WFPC2 sensitivity with each relevant filter curve. To derive a best-fitting value of the total-to-selective extinction ratio  $R$  in the presence of comparable relative error in both axes, we consider statistics within narrow slices of width 0.05 in residual intensity at  $B$  and evaluate the mean and median values of  $I$  residual intensity within these slices. The results are listed with standard deviations of the means, quartiles of the distributions, and modal estimates in Table 1 and are shown with a family of curves generated for  $R = 2.1$ – $4.1$  in Figure 10. The listed mode is the IRAF estimator, constructed by automatic binning and interpolation for such relatively sparse data sets. These statistics should be most useful in the middle of the extinction distribution, where, for example, the tilted cutoff at the high-extinction end will not bias the

TABLE 1  
DISTRIBUTION OF  $I$ -BAND TRANSMISSION  $T_I$  IN SLICES OF  $T_B$  FOR THE  
DUST IN AM 1316–241

$T_B$	Points	Mean	Median	25%	75%	Mode
0.10...	91	0.408 ± 0.010	0.397	0.340	0.463	0.309
0.15...	141	0.437 ± 0.007	0.438	0.374	0.494	0.351
0.20...	221	0.462 ± 0.006	0.458	0.397	0.527	0.440
0.25...	228	0.512 ± 0.005	0.519	0.453	0.564	0.549
0.30...	203	0.542 ± 0.006	0.545	0.492	0.598	0.543
0.35...	169	0.579 ± 0.006	0.582	0.542	0.629	0.583
0.40...	163	0.614 ± 0.007	0.611	0.562	0.665	0.613
0.45...	114	0.636 ± 0.008	0.637	0.588	0.698	0.657
0.50...	94	0.684 ± 0.008	0.687	0.620	0.743	0.717
0.55...	86	0.736 ± 0.008	0.748	0.678	0.796	0.760
0.60...	60	0.768 ± 0.012	0.780	0.730	0.824	0.795
0.65...	53	0.803 ± 0.010	0.813	0.762	0.839	0.836
0.70...	52	0.814 ± 0.015	0.812	0.781	0.861	0.813
0.75...	61	0.880 ± 0.008	0.881	0.844	0.911	0.882
0.80...	76	0.902 ± 0.007	0.898	0.874	0.937	0.875
0.85...	72	0.927 ± 0.005	0.918	0.900	0.952	0.909
0.90...	109	0.951 ± 0.005	0.953	0.910	0.995	0.993
0.95...	169	0.981 ± 0.003	0.986	0.960	1.006	0.989

results; we considered various ranges in  $B$ -band residual intensity for the fit. Using a  $\chi^2$  fit to the means (since mean values come with well-defined error bars), the range of residual intensity 0.15–0.90 yields the best fit, reduced  $\chi^2 = 2.3$  with one degree of freedom (the value of  $R$ ), namely,  $R = 3.6^{+0.5}_{-0.3}$ , where the error range is for 90% confidence. Since variation in  $R$  has a very constrained effect on the form of the curve, we also considered fits in which the top and bottom bins were included or excluded to test whether their errors, which are largely irreducible by changing  $R$ , dominate the overall statistic. In all cases, the 90% confidence bounds on  $R$  include the range 3.2–3.6, with preferred values 3.2–3.6. The  $\chi^2$ -values for these ranges are worse than the fiducial fit above. The value in AM 1316–241 is consistent with the Milky Way value, with some evidence that the extinction curve is slightly flatter ( $R$  greater) than the standard Galactic law. The dust follows a simple screen model much more closely than we found from ground-based data (WKC). This must be largely a resolution effect; at higher spatial resolution, we will see, the dust follows its intrinsic reddening law more closely as clumping becomes less important. There is marginal evidence for a smaller value of  $R$  at smaller extinction, with the formal fit for the residual intensity range 0.75–0.9 of  $R = 2.9$ . However, the number of fitting bins is small enough to make this at best a tentative statement.

We do see direct evidence for the effective reddening law changing at different resolutions when going to larger scales than the WFPC2 pixels, which accounts for the grayer extinction found from ground-based data (WKC). Block-averaging the transmission images to lower resolution shows a transition to a fitted value  $R = 4.1$  between 0".4 and 0".8 pixel sizes. Effective pixel sizes 0".2–0".4 yield color distributions that are consistent with the  $R$ -value fit to the original pixels. The transition between  $R$ -values that appear representative of the physical grain properties seen at the full data resolution and the artificially gray  $R$ -values we saw from the ground mostly takes place in the range from 200 to 400 pc resolution.

The color behavior in AM 0500–620 is broadly consistent with what we see in AM 1316–241, but less well-

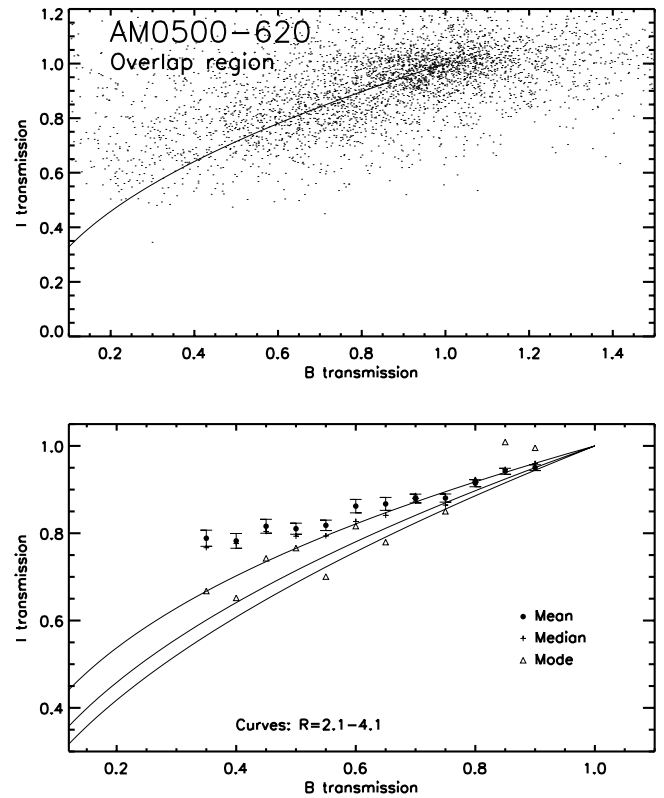


FIG. 11.—Same as Fig. 10, but for pixels in the overlapped region of AM 0500–620. Only the modal values yield fits at all consistent with the Galactic curve.

determined. The signal-to-noise ratio of the extinction in each pixel is lower by almost a factor of 2, so the scatter in the two-band transmission plot (Fig. 11) is larger than that for AM 1316–241. This is due both to weaker background light and to a larger contribution from foreground light in the spiral, which introduces a larger error in correction. A formal  $\chi^2$  fit to statistics in bins of  $B$  transmission (Table 2), as done for AM 1316–241, yields a 90% confidence interval of  $R = 1.5 \pm 0.4$  and the best-fitting  $\chi^2 = 2.5$  per degree of freedom, a poor fit. At face value, the dust in AM 0500–620 has a much smaller total-to-selective extinction ratio than Galactic grain populations. This behavior is in

TABLE 2  
DISTRIBUTION OF  $I$ -BAND TRANSMISSION  $T_I$  IN SLICES OF  $T_B$  FOR THE  
DUST IN AM 0500–620

$T_B$	Points	Mean	Median	25%	75%	Mode
0.35...	73	0.789 ± 0.019	0.767	0.690	0.921	0.668
0.40...	72	0.782 ± 0.017	0.776	0.652	0.883	0.652
0.45...	92	0.816 ± 0.016	0.804	0.703	0.913	0.743
0.50...	114	0.810 ± 0.013	0.793	0.720	0.874	0.766
0.55...	127	0.818 ± 0.012	0.794	0.718	0.894	0.701
0.60...	148	0.862 ± 0.015	0.827	0.745	0.942	0.816
0.65...	198	0.867 ± 0.015	0.841	0.764	0.939	0.780
0.70...	175	0.880 ± 0.010	0.873	0.793	0.975	0.886
0.75...	222	0.881 ± 0.009	0.865	0.787	0.959	0.850
0.80...	230	0.915 ± 0.008	0.921	0.828	0.991	0.923
0.85...	258	0.942 ± 0.007	0.946	0.872	1.009	1.009
0.90...	295	0.950 ± 0.007	0.960	0.902	1.017	0.996

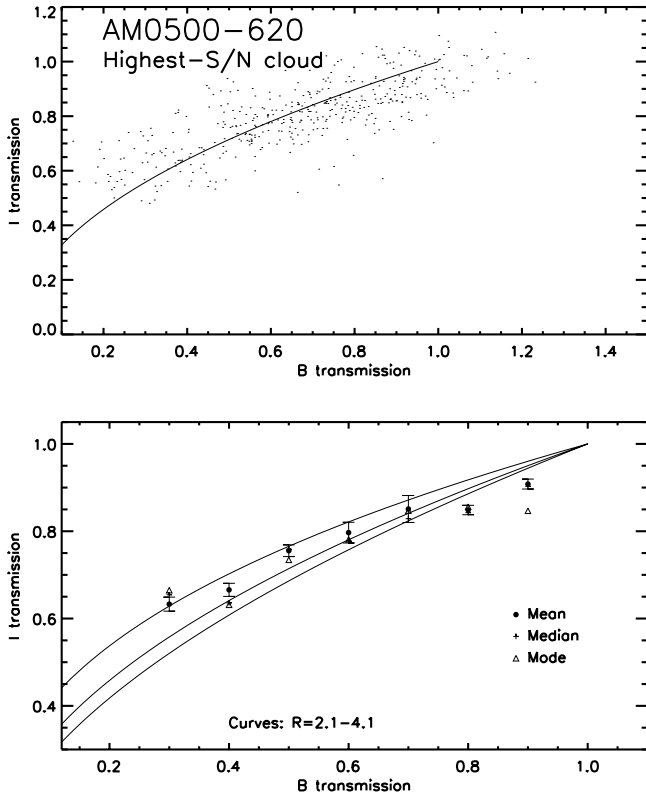


FIG. 12.—Same as Fig. 10, but for pixels in the dust cloud with highest S/N in AM 0500–620. These results are more consistent with local dust properties (albeit having substantial error bars) than with the wider area data of Fig. 10, perhaps indicating that systematic errors have crept in to the lower quality measures.

the wrong sense to be caused by either scattering or young stars, unless they are both highly reddened and distributed in such a way as to show no bright or very red structures in color-ratio images. The distribution of  $T_I$  in a narrow range of  $T_B$  is quite asymmetric in this object, as seen from the systematic differences among mean, median, and mode estimates in Figure 11. The peak of the distribution, shown by the modal behavior, most nearly tracks the  $R = 2-4$  curves, but even in this case the match is no more than broadly consistent. Repeating the procedure for only the single dust complex with the best-determined extinction values (Table 3; Fig. 12) yields results more consistent with the Galactic mean for all three measures (mean, median, mode) and the value  $R = 2.5 \pm 0.4$ , which may indicate that the results from the whole overlap region are less trustworthy.

We also examined the two-color reddening behavior in NGC 1275, restricting the analysis to pixels covering a total

TABLE 3

DISTRIBUTION OF  $I$ -BAND TRANSMISSION  $T_I$  IN SLICES OF  $T_B$  FOR AN ISOLATED DUST CLOUD IN AM 0500–620

$T_B$	Points	Mean	Median	25%	75%	Mode
0.30...	26	0.633 ± 0.016	0.654	0.545	0.709	0.665
0.40...	34	0.666 ± 0.015	0.636	0.607	0.701	0.631
0.50...	49	0.755 ± 0.013	0.759	0.709	0.821	0.735
0.60...	62	0.797 ± 0.024	0.776	0.724	0.822	0.781
0.70...	75	0.851 ± 0.031	0.829	0.778	0.878	0.847
0.80...	58	0.849 ± 0.011	0.843	0.806	0.888	0.856
0.90...	62	0.908 ± 0.011	0.903	0.855	0.981	0.847

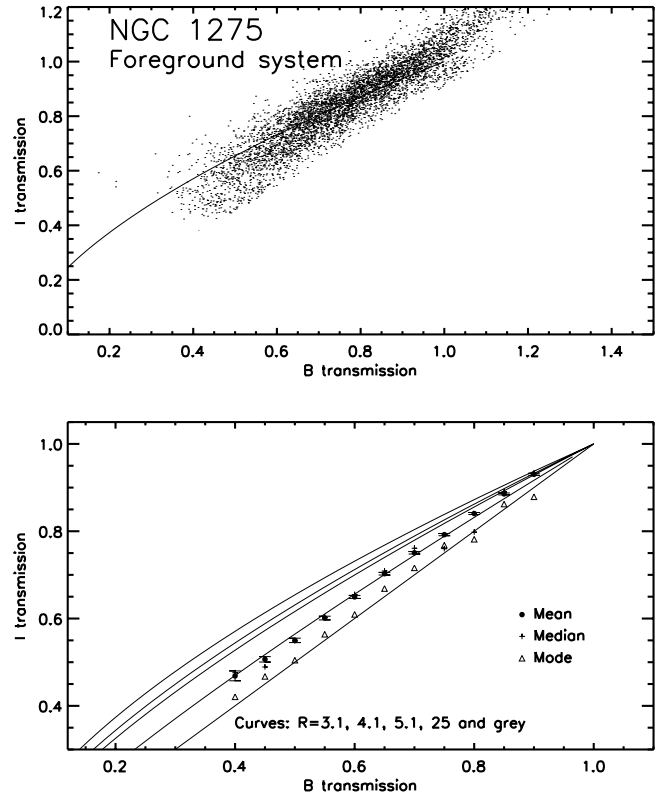


FIG. 13.—Two-band extinction relation for pixels that pass our color criterion to reduce foreground contamination in NGC 1275. The relation is much grayer than either what was found for the two AM galaxies or the Galactic mean. The two-color curves are slightly different here from in the other cases because F702W instead of F814W was used as the  $I$ -band filter. Curves are plotted for fiducial  $R$ -values to allow direct comparison with the other systems, at  $R = 4.1 \pm 1.0$ , as well as the high value  $R = 25$  in the middle of the acceptable fitting range from  $\chi^2$ , and with the straight line corresponding to gray extinction ( $R = \infty$ ).

area of 55 arcsec<sup>2</sup> from seven rectangular regions, including obvious dust features and excluding pixels masked by a color criterion intended to reduce contamination from (presumably blue) foreground starlight. The results are not consistent with a Galactic law (Table 4; Fig. 13). This could mean that we are unable to remove the foreground light even with a color criterion, that the dust in the foreground system of NGC 1275 is quite different from Milky Way

TABLE 4

DISTRIBUTION OF  $I$ -BAND TRANSMISSION  $T_I$  IN SLICES OF  $T_B$  FOR ABSORPTION REGIONS IN NGC 1275

$T_B$	Points	Mean	Median	25%	75%	Mode
0.40...	58	0.469 ± 0.011	0.426	0.476	0.552	0.421
0.45...	143	0.507 ± 0.006	0.471	0.489	0.611	0.467
0.50...	208	0.550 ± 0.005	0.516	0.549	0.648	0.505
0.55...	311	0.601 ± 0.004	0.566	0.603	0.703	0.564
0.60...	376	0.649 ± 0.004	0.619	0.655	0.744	0.609
0.65...	516	0.703 ± 0.003	0.671	0.709	0.797	0.669
0.70...	582	0.751 ± 0.003	0.719	0.761	0.844	0.716
0.75...	565	0.792 ± 0.002	0.768	0.760	0.840	0.768
0.80...	583	0.841 ± 0.002	0.818	0.798	0.873	0.782
0.85...	556	0.885 ± 0.002	0.866	0.890	0.953	0.862
0.90...	492	0.930 ± 0.002	0.913	0.933	0.996	0.879

dust, or that the foreground system actually lies well inside the stellar distribution of NGC 1275 proper. The  $R$ -parameter becomes ill-determined for extinction that is so nearly gray; in this instance, values of  $R$  in the range 18–35 are acceptable in a  $\chi^2$  sense when fitted to the mean values and statistical errors in Table 4.

#### 4. SUMMARY

We have used *HST* imaging of two spiral galaxies partially backlit by elliptical and S0 systems to provide direct measures of extinction and dust structure of the foreground spirals. This approach provides extinction estimates that are independent of the assumptions about internal structure that are necessary to perform many of the statistically based opacity tests often applied to this question.

Opacity maps show an interesting contrast between the spiral components of AM 1316–241 and those of AM 0500–620. In both cases, the arm-interarm dichotomy in extinction is strong. However, the statistics of coverage at various transmission levels are notably different in the two galaxies. The arm-interarm dichotomy in extinction is strengthened at the high resolution afforded by *HST*; much of what appeared in an earlier ground-based study as diffuse interarm dust is now seen to be composed of narrow spurs crossing the main spiral pattern (as in AM 0500–620). For the areas we can analyze, located at radii  $(0.4\text{--}0.8)R_{25}$ , the dust is heavily concentrated toward the arms, with half the dust mass contained in only 20% of the projected area and 95%–98% of the dust mass contained in half the area. Kiloparsec-scale complexes of absorbing material are estimated to contain  $(3\text{--}7) \times 10^4 M_\odot$  of dust grains, with correspondingly large implied gas masses,  $(1\text{--}2) \times 10^7 M_\odot$ , if we assume a typical Galactic gas-to-dust ratio. Interarm extinction is quite small, although the statistical distribution by area differs for the two spirals. There is a well-defined low-extinction peak in the areal distribution for AM 1316–241, while the distribution of extinction values is much broader and continuous with the arm regions in AM 0500–620.

Reddening curves have been measured by comparing transmitted light pixel-by-pixel between  $B$  and  $I$  passbands. For AM 1316–241, we find a well-determined slope, given by  $R = A_V/E(B-V) = 3.4 \pm 0.2$ , close to the Galactic value of 3.1 derived largely from diffuse regions. The data quality for AM 0500–620 is poorer, and the overall fit to a Galactic law (or any plausible reddening law) is poor. For the single cloud in AM 0500–620 with the best data, we do see reasonable reddening behavior, with a formal fit of  $R = 2.5 \pm 0.4$ . In NGC 1275, our accuracy is limited by our inability to estimate the brightness of the foreground galaxy. We have used a color criterion to eliminate pixels with obvious foreground light and find the remainder to have a reddening curve much flatter (grayer) than the local norm. This might imply a that the dust composition is different, the fine-scale distribution is different, or the foreground system is so close to NGC 1275 that it is at least partially embedded within its stellar distribution (so that our simple geometric scheme for measuring opacity fails).

We speculate, moreover, that the dust grain size distribution in the NGC 1275 foreground system has been truncated at the low end by sputtering in the hot intracluster medium of A426. Lack of particles smaller than  $\sim 0.5 \mu\text{m}$  would flatten the extinction curve effectively. Following Draine & Salpeter (1979), the survival timescale for particles

of radius  $a$  embedded in a hot medium of density  $n$  is

$$t_{\text{sp}} = 10^6 \frac{a}{n} \text{ yr},$$

for  $a$  in microns and  $n$  in  $\text{cm}^{-3}$ . For a representative value of  $n = 10^{-3}$ , the timescale for  $a = 0.25 \mu\text{m}$  is  $10^9$  yr. At the high-velocity difference between this system and NGC 1275 proper (itself essentially at rest in the cluster) it would have moved at least 3 Mpc during the time it would take to sputter a Galactic grain population to this extent. This is comparable to the extent of X-ray emission from the Perseus cluster (Ettori, Fabian, & White 1998). A strict application of this sputtering prescription would weight the distribution toward larger grains only for very specific size distributions, since for spherical grains and a power-law size distribution the net effect of sputtering would be to shrink all grains at a constant rate by area (rather than by volume). In this case, a given set of original grains would move down the size distribution in step, with the only net effect being progressive loss of the largest grains. However, recent modeling of sputtering effects on more realistic grain structures suggest that the net effect can indeed be a graying of the extinction curve (Aguirre 1999a). Furthermore, preferential ejection of small grains due to either ram pressure or galactic winds would weight the distribution toward larger sizes (Aguirre 1999b). If the grain population in the foreground system of NGC 1275 has indeed been altered, the original dust mass and typical  $B$  extinction would have been substantially larger than we observe (with the  $I$  extinction being less affected, since larger grains are more important at this wavelength). If the system has interacted with the intracluster medium, the small H I mass (van Gorkom & Ekers 1983) is easier to reconcile with the morphological evidence for a late Hubble type, since H I is the first ISM component lost from cluster spirals (Cayatte et al. 1990; Bravo-Alfaro et al. 2000).

We have used the perimeter-smoothing length test to see whether the dust in these galaxies can be well described by fractal (scale free) structures, as has been found for H I distributions in nearby spirals. We find scale-free behavior for the perimeter of a given contour in dust column density as a function of smoothing scale from 0.05 to 8 kpc. However, we cannot determine a fractal dimension from these data because the scaling between different contours (at different transmission levels) at a given smoothing length does not show the requisite linear relation for  $\log(\text{area})$  versus  $\log(\text{perimeter})$  relation (the perimeter in fact peaks within the measured area range). We can thus describe the dust distribution as fractal-like but not formally fractal, with box-counting dimension close to 1.4 but area-perimeter measures yielding dimensions near 0.7. The box-counting dimension is within the range found for H I structures in galaxies by Westpfahl et al. (1999), but given the discrepancy between the two dimensions and the non-monotonic area-perimeter relation the dust distribution cannot be accurately described as fractal. The area covered at a given extinction level is nearly independent of smoothing scale over the range we can measure, so that our dust mass estimates are not biased by structures smaller than our resolution.

What processes define and control fine structure in the dust? Grains are generally strongly coupled to other components of the interstellar medium, both empirically and for

robust theoretical reasons, so the dust distribution reflects a range of physical processes that need not have a direct impact on the grains. Strictly dynamical features of disk dynamics can concentrate the ISM into regions of high density and can change the configuration of these regions on dynamical timescales (a recently discussed example is amplification of small fluctuations as seen in the nuclear dust patterns of NGC 2207; Elmegreen et al. 1998). Energy input from stellar winds and supernovae has a crucial role in altering the small-scale structure of the ISM (Rosen & Bregman 1995), both mechanically and by driving phase changes (including grain evaporation in the most extreme environments). These data will not support a detailed analysis of such issues, but the differences in dust distributions may most plausibly be linked to changes in the energy

input rates and perhaps to different dominant mechanisms shaping the ISM in these two galaxies.

This work was supported by NASA *HST* grant GO 06438.01-95A. R. E. W. was supported in part by a National Research Council Senior Research Associateship at NASA/GSFC. We thank Dave Westpfahl for secret tips on doing the fractal index measurements within IRAF and Bruce Elmegreen for asking some especially probing questions. Wentao Wu provided the specific Bruzual-Charlot model spectra for rigorous extinction calculations. Alex Rosen pointed out the role of stellar energy input for the scales of ISM structures. We thank the referee for forcing us to clarify the role of noise in the dimensional analysis and actually state the implied fractal dimensions.

## REFERENCES

- Aguirre, A. 1999a, *ApJ*, 512, L19  
 ———, 1999b, *ApJ*, 525, 583  
 Arp, H. C., & Madore, B. F. 1987, *A Catalogue of Southern Peculiar Galaxies and Associations* (Cambridge: Cambridge Univ. Press)  
 Bravo-Alfaro, H., Cayatte, V., van Gorkom, J. H., & Balkowski, C. 2000, *AJ*, 119, 580  
 Burstein, D., Haynes, M. P., & Faber, S. M. 1991, *Nature*, 353, 515  
 Cardelli, J. A., Clayton, G. C., & Mathis, J. S. 1989, *ApJ*, 345, 245  
 Carlson, M. N., et al. 1998, *AJ*, 115, 1778  
 Cayatte, V., Balkowski, C., van Gorkom, J. H., & Kotanyi, C. 1990, *AJ*, 100, 604  
 Charlot, S., & Bruzual A. G. 1991, *ApJ*, 367, 126  
 Curtis, H. D. 1918, *Publ. Lick Obs.*, 13  
 Disney, M. J., Davies, J., & Phillipps, S. 1989, *MNRAS*, 239, 939  
 Domingue, D. L., Keel, W. C., Ryder, S. D., & White, R. E., III. 1999, *AJ*, 118, 1542  
 Donzelli, C. J., & Pastoriza, M. G. 2000, *AJ*, 120, 189  
 Draine, B. T., & Salpeter, E. E. 1979, *ApJ*, 2231, 77  
 Elmegreen, B. G., et al. 1998, *ApJ*, 503, L119  
 Ettori, S., Fabian, A. C., & White, D. A. 1998, *MNRAS*, 300, 837  
 Holmberg, E. 1958, *Medd. Lunds Astron. Obs.*, Ser. 2, 136  
 Hu, E. M., Cowie, L. L., Kaaret, P., Jenkins, E. B., York, D. G., & Roesler, F. L. 1983, *ApJ*, 275, L27  
 Keel, W. C. 1983, *AJ*, 88, 1579  
 Keel, W. C., & White, R. E., III. 1995, in *The Opacity of Spiral Disks*, ed. J. I. Davies & D. Burstein (Dordrecht: Kluwer), 167  
 Lauberts, A., & Valentijn, E. A. 1989, *The Surface Photometry Catalog of the ESO-Uppsala Galaxies* (Garching: ESO)  
 Rosen, A., & Bregman, J. N. 1995, *ApJ*, 440, 634  
 Valentijn, E. A. 1990, *Nature*, 346, 153  
 van Gorkom, J. H., & Ekers, R. D. 1983, *ApJ*, 267, 528  
 Westpfahl, D. J., Coleman, P. H., Alexander, J., & Tongue, T. 1999, *AJ*, 117, 868  
 White, R. E., III, & Keel, W. C. 1992, *Nature*, 359, 129  
 White, R. E., III, Keel, W. C., & Conselice, C. J. 1996, in *New Extragalactic Perspectives in the New South Africa*, ed. D. L. Block & J. M. Greenberg (Dordrecht: Kluwer), 114  
 ———. 2000, *ApJ*, 542, 761 (WKC)